

MoDIR: Motion-Compensated Training for Deep Image Reconstruction without Ground Truth

Weijie Gan^{*}, Yu Sun^{*}, Cihat Eldeniz[†], Jiaming Liu[‡], Hongyu An[§], Ulugbek S. Kamilov[¶]

Abstract

Deep neural networks for medical image reconstruction are traditionally trained using high-quality ground-truth images as training targets. Recent work on *Noise2Noise (N2N)* has shown the potential of using multiple noisy measurements of the same object as an alternative to having a ground truth. However, existing N2N-based methods cannot exploit information from various motion states, limiting their ability to learn on moving objects. This paper addresses this issue by proposing a novel *motion-compensated deep image reconstruction (MoDIR)* method that can use information from several *unregistered and noisy measurements* for training. MoDIR deals with object motion by including a deep registration module jointly trained with the deep reconstruction network without any ground-truth supervision. We validate MoDIR on both simulated and experimentally collected *magnetic resonance imaging (MRI)* data and show that it significantly improves imaging quality.

1 Introduction

The recovery of a high-quality image from a set of noisy measurements is fundamental in medical imaging. For instance, it is essential in *compressed sensing magnetic resonance imaging (CS-MRI)* [1], which aims at obtaining diagnostic-quality images from severely undersampled k-space measurements. The recovery is traditionally formulated as an *inverse problem* that leverages a forward model characterizing the physics of data acquisition and a regularizer imposing prior knowledge on the solution. Many regularizers have been proposed to date, including those based on transform-domain sparsity, low-rank penalty, and dictionary learning [3–6].

Deep learning (DL) has recently gained popularity in medical image reconstruction [7–11]. A widely used DL strategy is based on training a *convolutional neural network (CNN)* to map a low-quality image to its desired high-quality counterpart. However, this simple supervised DL approach is impractical in applications where it is difficult to collect a sufficient number of high-quality training images. This limitation has motivated the research on “ground-truth-free” DL schemes that rely exclusively on the information available in the corrupted data itself [2, 12–15]. In this study, we focus on the line of work based on *Noise2Noise (N2N)* [13], which has shown that one can train a CNN without ground truth by using only pairs of noisy observations of the same object. Recent extensions to N2N have investigated the potential of this strategy in a variety of imaging scenarios [16–24].

^{*}Weijie Gan and Yu Sun are with the Department of Computer Science & Engineering, Washington University in St. Louis, St. Louis, MO 63130 USA (e-mail: weijie.gan@wustl.edu; sun.yu@wustl.edu).

[†]Cihat Eldeniz is with the Mallinckrodt Institute of Radiology, Washington University in St. Louis, St. Louis, MO 63130 USA (e-mail: cihat.eldeniz@wustl.edu).

[‡]Jiaming Liu is with the Department of Electrical & System Engineering, Washington University in St. Louis, St. Louis, MO 63130 USA (e-mail: jiaming.liu@wustl.edu).

[§]Hongyu An is with the Mallinckrodt Institute of Radiology, Department of Neurology, Department of Biomedical Engineering, Saint Louis, MO 63130 USA, and also with the Division of Biology and Biomedical Sciences, Washington University in St. Louis, St. Louis, MO 63130 USA (e-mail: hongyuan@wustl.edu).

[¶]Ulugbek S. Kamilov is with the Department of Computer Science & Engineering and Electrical & Systems Engineering, Washington University in St. Louis, St. Louis, MO 63130 USA (e-mail: kamilov@ieee.org).

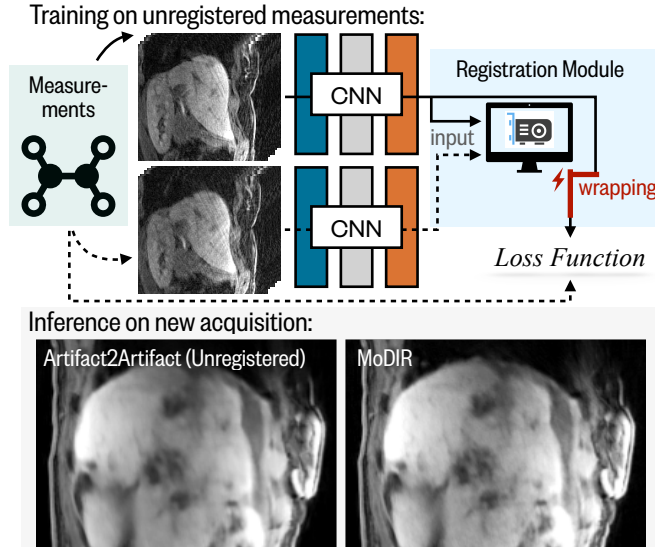


Figure 1: The conceptual illustration of MoDIR for CS-MRI [1]. MoDIR trains a *convolutional neural network (CNN)* on unregistered measurements using a registration module that corrects for object motion. This visual example highlights the improvement of MoDIR over the *Artifact2Artifact (A2A)* [2] method that learns directly from the raw measurements without any motion compensation.

Despite the recent progress, current N2N-based methods inherently assume that the object is stationary across all the measurements. This assumption limits the ability to exploit information from multiple measurements of the same object with different motion states. To overcome this limitation, we propose a novel *motion-compensated deep image reconstruction (MoDIR)* method that uses multiple motion-affected measurements of an object by integrating a deep registration [25] module into our deep architecture for an end-to-end training. MoDIR enables training without any ground-truth supervision by adopting recent ideas from self-supervised deep registration [26–29]. In short, The key features of MoDIR are as follows:

- MoDIR builds on *Artifact2Artifact (A2A)* [2], which extends N2N to enable learning from undersampled and noisy measurements. MoDIR is directly trained in the measurement domain (e.g., k-space for MRI) by transforming the reconstructed images back to the measurement domain and minimizing the difference between the predicted measurements and the measured raw data, without any fully sampled ground truth.
- Unlike A2A and N2N, MoDIR can exploit information from multiple measurements of an object undergoing nonrigid deformation. This capability is achieved by integrating a deep registration module into the final architecture (see Fig. 2), which is trained end-to-end on unregistered, noisy, and subsampled measurements. Note that the registration module is only necessary during training, since image reconstruction can be performed by using only the reconstruction module.
- MoDIR achieves excellent performance on simulated and experimentally collected MRI data. Our simulation results show that MoDIR quantitatively matches the performance of A2A that is fully informed of the object motion. Our results on experimentally collected data show that MoDIR leads to a significant quality improvements by using measurements with different motion states.

This paper extends the preliminary work [30] presented at the 2021 IEEE International Symposium on Biomedical Imaging by including additional technical details and validation on experimentally collected MRI data.

2 Background

2.1 Imaging Inverse Problems

We consider the problem of recovering an unknown image $\mathbf{x} \in \mathbb{C}^n$ from its noisy measurements $\mathbf{y} \in \mathbb{C}^m$ specified by the linear system

$$\mathbf{y} = \mathbf{H}\mathbf{x} + \mathbf{e} , \quad (1)$$

where $\mathbf{e} \in \mathbb{C}^m$ is noise and $\mathbf{H} \in \mathbb{C}^{m \times n}$ is the measurement operator that characterizes the response of the imaging system. For instance, \mathbf{H} in parallel CS-MRI with a dynamic object can be represented as

$$\mathbf{H}_i^{(t)} = \mathbf{P}^{(t)} \mathbf{F} \mathbf{S}_i , \quad (2)$$

where \mathbf{F} denotes the Fourier transform operator, $\mathbf{P}^{(t)}$ refers to a k-space sampling operator at time t , and \mathbf{S}_i is the matrix of the pixel-wise sensitivity map of the i th coil. When the inverse problem is ill-posed (e.g., for $m < n$), inverse problems are conventionally formulated as regularized optimization

$$\arg \min_{\mathbf{x} \in \mathbb{C}^n} g(\mathbf{x}) + h(\mathbf{x}) , \quad (3)$$

where g is the data-fidelity term that quantifies consistency with the observed data \mathbf{y} and h is a regularizer that encodes prior knowledge on \mathbf{x} . For example, two widely used functions in imaging are the least-squares and total variation (TV)

$$g(\mathbf{x}) = \frac{1}{2} \|\mathbf{H}\mathbf{x} - \mathbf{y}\|_2^2 \quad \text{and} \quad h(\mathbf{x}) = \tau \|\mathbf{D}\mathbf{x}\|_1 , \quad (4)$$

where $\tau > 0$ controls the regularization strength and \mathbf{D} is the discrete gradient operator [6].

In the past few years, DL has gained popularity for solving imaging inverse problems due to its excellent performance (see reviews in [7–11]). One widely-used DL approach is based on training a CNN $h_\theta(\cdot)$, with parameters $\theta \in \mathbb{R}^p$, to compute a regularized inverse of \mathbf{H} by mapping corrupted images to their clean target versions. The training can be formulated as an optimization problem

$$\arg \min_{\theta} \sum_i \mathcal{L}(h_\theta(\mathbf{H}_i^\dagger \mathbf{y}_i), \mathbf{x}_i) , \quad (5)$$

where \mathbf{H}^\dagger is an approximate inverse of \mathbf{H} , \mathcal{L} is a loss function, and i indexes the samples in the training set. Popular choices for \mathcal{L} include the ℓ_1 and ℓ_2 norms. For example, prior work on DL for CS-MRI has trained the CNN by mapping the zero-filled images to their corresponding fully-sampled ground-truth images [31–33]. While traditional DL relies on generic CNN architectures (such as UNet [34]), recent work has also explored the integration of DL and model-based optimization. For example, *plug-and-play priors (PnP)* [35] and *regularization by denoisers (RED)* [36] refer to a related family of algorithms that use pre-trained deep denoisers as imaging priors [37–40]. The recent publication [41] has reviewed PnP/RED in the context of image reconstruction for MRI. *Deep unrolling* is another widely-used strategy inspired by LISTA [42], where the iterations of a regularized optimization are interpreted as layers of a CNN and trained in an end-to-end fashion [31–33, 42–45].

Our work contributes to this broad area by providing a new DL method that does not require clean ground-truth images as training targets. While this work focuses on traditional model-free DL architectures, our method is fully compatible with the latest model-based architectures.

2.2 Image reconstruction based on Noise2Noise

There is a growing interest in DL image reconstruction to reduce the dependence on high-quality ground-truth training targets. One widely-adopted framework is *N2N* [13], where the CNN h_θ is trained on a group of noisy images $\{\hat{\mathbf{x}}_{ij}\}$, with j indexing different realizations of the same underlying image i . There have been multiple extensions of the original method [16–24] with applications to numerous medical imaging

problems, including motion-resolved MRI [2, 17], cryo-transmission electron microscopy (cryo-TEM) [22] and optical coherence tomography angiography (OCTA) [21]. A2A [2] is one of the extensions of N2N that showed excellent performance using multiple noisy and artifact-corrupted images $\{\hat{\mathbf{x}}_{ij}\}$ obtained directly from sparsely-sampled MR measurements. In A2A, ij denotes the j^{th} MRI acquisition of the subject i with each acquisition consisting of an independent undersampling pattern and noise realization. The CNN is trained by minimizing a loss function

$$\arg \min_{\theta} \sum_{i,j,j'} \mathcal{L}(h_{\theta}(\hat{\mathbf{x}}_{ij}), \hat{\mathbf{x}}_{ij'}). \quad (6)$$

Recent work [15] showed the potential of training a model-based deep network without ground truth by dividing a single k-space MRI acquisition into two subsets and using both subsampled sets of measurements as training targets. A similar strategy has also been used for denoising in 3D parallel-beam tomography by splitting a stack of noisy sinograms along the angular axis [23]. Two recent papers considered the inclusion of image deformation into the training of a deep image denoiser [20, 24]. In [20], a pre-trained registration network is used for training a video denoising network. In [24], a deep network is trained along with a deep deformation network to remove common types of noise in medical images, including additive white Gaussian noise (AWGN), Rician noise, and Poisson noise. The key difference of our work is that it goes beyond denoising by considering general inverse problems and using training labels directly in the k-space for MRI.

Noise2Void [14] refers to a related family of methods [46–48] that use a dataset of noisy images containing a single copy of each for training. Similarly, *Self2Self* [49] extends this idea to use only a single noisy image as a training sample. These methods have been shown to achieve excellent performance in the context of image denoising. However, the advantage of using only a single realization of each image in training comes with the limitation that the noise (or the artifact-pattern) over the image has to be incoherent in order to differentiate it from the features of the object.

Our work contributes to this area by enabling the use of information from the various measurements of the object at different motion states. It not only allows our method to use more information for training, but it also defies the assumptions of stationarity and artifact incoherence made by the previous studies. While our focus is on the traditional CNN architectures, our work can be combined with [15] to enable model-based DL.

2.3 Deep Image Registration

Let r and m denote a reference image and its deformed counterpart, respectively. Deformable image registration aims to obtain a registration field $\hat{\phi}^{m \rightarrow r}$ that maps the coordinates of m to those of r by comparing the content of the corresponding images. Deformable image registration has been widely used in many applications, such as motion tracking [50] and image segmentation [51, 52]. The registration field $\hat{\phi}^{m \rightarrow r}$ is often characterized by a displacement vector field $\hat{v}^{m \rightarrow r}$ that represents coordinate offsets from m to r , $\hat{\phi}^{m \rightarrow r} = \mathbf{I} + \hat{v}^{m \rightarrow r}$, where \mathbf{I} denotes an identity transformation [53].

Recently, there has been considerable interest in developing DL methods for deformable image registration [25], especially methods that require no knowledge of the ground-truth transformation for training [26–29]. The corresponding self-supervised methods train a CNN g_{φ} , with parameters $\varphi \in \mathbb{R}^k$, by mapping an input image pair $\{m, r\}$ to a deformation field $\hat{\phi}^{m \rightarrow r} = g_{\varphi}(m, r)$ that can be used for registration [25]. The CNN is trained on a set of image pairs $\{m_i, r_i\}$ by minimizing the following loss function

$$\arg \min_{\varphi} \sum_i \mathcal{L}_d(m_i \circ \hat{\phi}_i^{m \rightarrow r}, r_i) + \mathcal{L}_r(\hat{\phi}_i^{m \rightarrow r}), \quad (7)$$

where \circ is the warping operator that transforms the coordinates of m_i based on the registration field $\hat{\phi}_i^{m \rightarrow r}$. The term \mathcal{L}_d penalizes the discrepancy between m_i after transformation and its reference r_i , while \mathcal{L}_r regularizes the local spatial variations in the estimated registration field. In order to use the standard gradient

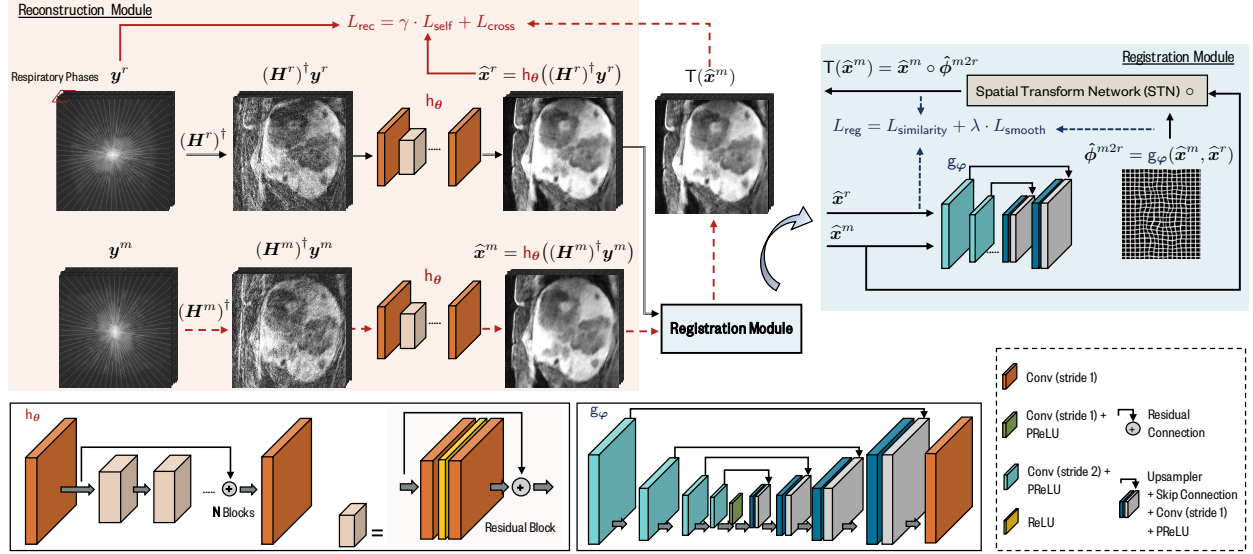


Figure 2: The proposed method jointly trains two CNN modules: h_θ for image reconstruction and g_φ for image registration. Inputs are the measurement pairs of the same object but at different motion states. The zero-filled images are passed through h_θ to remove artifacts due to noise and undersampling. The output images are then used in g_φ to obtain the motion field characterizing the directional mapping between their coordinates. We implement the warping operator as the *Spatial Transform Network (STN)* to register one of the reconstructed images to the other. We train the whole network end-to-end without any ground-truth images or transformations.

Algorithm 1 Training procedure of MoDIR

Require: Initial parameters θ^0 and φ^0 , total number of iterations K , and two Adam [55] optimizers Adam_{rec} and Adam_{reg} .

- 1: **for** number of training iterations $k = 1, 2, \dots, K$ **do**
- 2: Select a training mini-batch: $\mathbf{y}_i^r, \mathbf{y}_i^m, \mathbf{H}_i^r, \mathbf{H}_i^m$
- 3: $\theta^k \leftarrow \text{Adam}_{\text{rec}}(\theta^{k-1}, \partial L_{\text{rec}} / \partial \theta)$
- 4: $\varphi^k \leftarrow \text{Adam}_{\text{reg}}(\varphi^{k-1}, \partial L_{\text{reg}} / \partial \varphi)$
- 5: **end for**
- 6: **return** Learned parameters θ^K and φ^K .

methods for minimizing this loss function, the warping operator needs to be differentiable and is often implemented as the *Spatial Transform Network (STN)* [54].

Our work seeks to leverage the recent progress in deep image registration to enable a novel methodology for training deep reconstruction networks on motion-affected datasets.

3 Proposed Method

In this section, we introduce the technical details of the proposed method. We start by describing the overall architecture, followed by the details of each module.

3.1 Overall Model

Consider a pair of unregistered measurements $(\mathbf{y}^r, \mathbf{y}^m)$ obtained separately from the same object

$$\mathbf{y}^r = \mathbf{H}^r \mathbf{x}^r + \mathbf{e}^r \text{ and} \tag{8a}$$

$$\mathbf{y}^m = \mathbf{H}^m \mathbf{x}^m + \mathbf{e}^m \text{ with } \mathbf{x}^m = \mathbf{x}^r \circ \phi^{r \rightarrow m}, \tag{8b}$$

where $(\mathbf{H}^r, \mathbf{H}^m)$ and $(\mathbf{e}^r, \mathbf{e}^m)$ denote distinct forward operators and noise vectors, respectively. Eq. (8b) models the object motion as a dense nonrigid transformation-field $\phi^{r \rightarrow m}$ relative to \mathbf{x}^r . For example, $(\mathbf{y}^r, \mathbf{y}^m)$ can be two motion-affected accelerated MRI measurements of the same patient. Our method aims to train a deep neural network on a set of such pairs $\{(\mathbf{y}_i^r, \mathbf{y}_i^m)\}_i^N$, where $N \geq 1$ denotes the total number of training samples, without the need for ground-truth images (\mathbf{x}_i^r and \mathbf{x}_i^m) or transformations ($\phi_i^{r \rightarrow m}$).

Fig. 2 summarizes the data processing pipeline of MoDIR. It consists of a reconstruction module trained to form images from measurements, and a registration module for registering the reconstructed images onto each other. The trainable parameters of both modules are denoted as θ and φ in respective order. During training, we define two distinct loss functions \mathcal{L}_{rec} and \mathcal{L}_{reg} as well as two Adam [55] optimizers Adam_{rec} and Adam_{reg} for each module. Given a mini-batch of training samples, the proposed training procedure alternatively minimizes the loss functions by fixing the trainable parameters of one module while training the other. Algorithm 1 summarizes the training strategy. Note that the registration module of MoDIR is only employed during training, since reconstruction during testing can be performed directly by using the reconstruction module alone.

3.2 Reconstruction Module

During training, the reconstruction module separately takes two measurements \mathbf{y}^r and \mathbf{y}^m described in (8) as inputs to produce two images $\hat{\mathbf{x}}^r$ and $\hat{\mathbf{x}}^m$ as outputs, respectively. The measurements are first mapped to the image domain by applying the approximate inverses of their respective forward operators. We denote with $(\mathbf{H}^m)^\dagger \mathbf{y}^m$ and $(\mathbf{H}^r)^\dagger \mathbf{y}^r$ the resulting artifact-corrupted images in the image domain. A CNN h_θ with parameters $\theta \in \mathbb{R}^p$ is then trained to remove the artifacts from the corrupted images

$$\hat{\mathbf{x}}^m = h_\theta((\mathbf{H}^m)^\dagger \mathbf{y}^m) \text{ and } \hat{\mathbf{x}}^r = h_\theta((\mathbf{H}^r)^\dagger \mathbf{y}^r). \tag{9}$$

Our network is a customized version of the residual CNN used in the prior work on deep image reconstruction [2, 15, 56].

Since the images $\hat{\mathbf{x}}^m$ and $\hat{\mathbf{x}}^r$ are not aligned due to the deformation $\phi^{m \rightarrow r}$, we cannot directly compare them during training. It is thus necessary to use the registration module to mitigate their potential misalignment. We define $\mathbf{T}(\hat{\mathbf{x}}^r)$ and $\mathbf{T}(\hat{\mathbf{x}}^m)$ as the images transformed according to the estimated deformation field (see details in Sec. 3.3). In our notation, $\mathbf{T}(\hat{\mathbf{x}}^r)$ denotes a transformed variant of $\hat{\mathbf{x}}^r$ relative to $\hat{\mathbf{x}}^m$.

The loss function \mathcal{L}_{rec} of h_θ has two components

$$\mathcal{L}_{\text{rec}} = \mathcal{L}_{\text{cross}} + \gamma \cdot \mathcal{L}_{\text{self}}, \tag{10}$$

where the parameter $\gamma > 0$ controls the relative strength of each component. The function $\mathcal{L}_{\text{cross}}$ is the main component that penalizes the difference between the raw data and the transformed reconstructed image at a different motion state

$$\mathcal{L}_{\text{cross}} = \sum_{i=1}^N \mathcal{L}(\mathbf{y}_i^r, \mathbf{H}_i^r \mathbf{T}(\hat{\mathbf{x}}_i^m)) + \mathcal{L}(\mathbf{y}_i^m, \mathbf{H}_i^m \mathbf{T}(\hat{\mathbf{x}}_i^r)), \tag{11}$$

where \mathbf{H}_i^m and \mathbf{H}_i^r are the forward operators used to map the registered images back to the measurement domain. Eq. (11) maps pairs of measurements having the forms (8a) and (8b) by assuming that the deformations between them have been accounted for via the registration module. The function $\mathcal{L}_{\text{self}}$ penalizes the

discrepancy between the measurements estimated from a reconstructed image and the corresponding actual raw measurements

$$\mathcal{L}_{\text{self}} = \sum_{i=1}^N \mathcal{L}(\mathbf{y}_i^r, \mathbf{H}_i^r \hat{\mathbf{x}}_i^r) + \mathcal{L}(\mathbf{y}_i^m, \mathbf{H}_i^m \hat{\mathbf{x}}_i^m). \quad (12)$$

Note that N2N/A2A can be seen as special cases of the proposed method where the potential deformations between the measurements are set to identity.

3.3 Registration Module

Our registration module builds on self-supervised deep image registration discussed in Sec. 2.3, which consists of a CNN g_φ , customized from U-net [34] with trainable parameters $\varphi \in \mathbb{R}^q$, and a *Spatial Transform Network (STN)* [54]. As its order-sensitive input, the network accepts a pair of reconstructed images $(\hat{\mathbf{x}}^m, \hat{\mathbf{x}}^r)$ estimated using h_θ and registers them onto each other. The network g_φ uses two inputs in different orders to generate two motion fields

$$\hat{\phi}^{m \rightarrow r} = g_\varphi(\hat{\mathbf{x}}^m, \hat{\mathbf{x}}^r) \text{ and } \hat{\phi}^{r \rightarrow m} = g_\varphi(\hat{\mathbf{x}}^r, \hat{\mathbf{x}}^m) \quad (13)$$

that characterize two coordinate mappings with opposite directions relative to each other. For example, $\hat{\phi}^{m \rightarrow r}$ denotes a directional mapping from the coordinates of $\hat{\mathbf{x}}^m$ to those of $\hat{\mathbf{x}}^r$. STN then transforms the coordinate of inputs based on the motion fields and obtains their registered variants

$$\mathbf{T}(\hat{\mathbf{x}}^m) = \hat{\mathbf{x}}^m \circ \hat{\phi}^{m \rightarrow r} \text{ and } \mathbf{T}(\hat{\mathbf{x}}^r) = \hat{\mathbf{x}}^r \circ \hat{\phi}^{r \rightarrow m}. \quad (14)$$

The loss function \mathcal{L}_{reg} for training g_φ is specified as

$$\mathcal{L}_{\text{reg}} = \mathcal{L}_{\text{similarity}} + \lambda \cdot \mathcal{L}_{\text{smooth}}, \quad (15)$$

where $\mathcal{L}_{\text{similarity}}$ enforces similarity between registered images and their references, $\mathcal{L}_{\text{smooth}}$ enforces spatial smoothness in the motion field, and $\lambda > 0$ is a regularization parameter. The function $\mathcal{L}_{\text{similarity}}$ is given by

$$\mathcal{L}_{\text{similarity}} = - \sum_i (\text{LCC}(\mathbf{T}(\hat{\mathbf{x}}^m), \hat{\mathbf{x}}_i^r) + \text{LCC}(\mathbf{T}(\hat{\mathbf{x}}^r), \hat{\mathbf{x}}_i^m)). \quad (16)$$

where LCC denotes the local cross-correlation (LCC) [29], which is known to be robust to intensity variations across different acquisitions [57]. While minimizing $\mathcal{L}_{\text{similarity}}$ enforces accurate alignment, it can also generate non-smooth registration fields that are not physically realistic [29]. Therefore, we include the function $\mathcal{L}_{\text{smooth}}$ that imposes smoothness on the coordinate offsets $\hat{\mathbf{v}} = \hat{\phi} - \mathbf{I}$

$$\mathcal{L}_{\text{smooth}} = \sum_i \left(\|\mathbf{D}\hat{\mathbf{v}}_i^{m \rightarrow r}\|^2 + \|\mathbf{D}\hat{\mathbf{v}}_i^{r \rightarrow m}\|^2 \right). \quad (17)$$

4 Numerical Validation

We now test our method in the context of accelerated MRI. We consider three settings: (a) *2D simulated measurements and simulated deformations*; (b) *2D simulated measurements and real unknown deformations*; and (c) *3D experimentally collected measurements and real unknown deformations*.

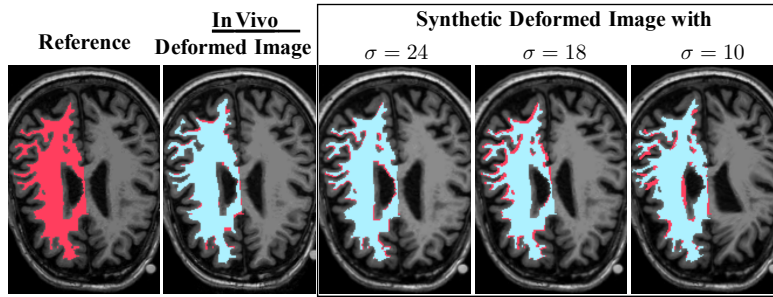


Figure 3: Visual illustration of deformations in the simulated experiments. The red regions are segmentations in the reference, while the blue regions are the corresponding segmentations in the deformed counterparts. The synthetic deformations were generated by using the method in [58], where σ is inversely related to the deformation strengths. The *in vivo* deformation is due to normal aging and disease.

Table 1: Average PSNR and SSIM values over the test set. The table highlights that MoDIR outperforms several baseline methods and achieves comparable performance to the idealized A2A (*Oracle*) method, which uses the true deformations.

Experiment of Simulated Measurement and Simulated Deformation												
Schemes	PSNR						SSIM					
	10		18		24		10		18		24	
<i>Synthetic Deformable with $\sigma =$</i>	x3	x4										
Acceleration rate												
Zero-Filled (ZF)	28.20	26.03	28.19	26.02	28.28	26.05	0.772	0.717	0.772	0.715	0.774	0.716
Total Variation	33.01	29.78	32.96	29.79	33.18	29.82	0.942	0.893	0.941	0.893	0.944	0.894
A2A (Unregistered)	30.19	29.07	31.96	30.37	32.83	30.89	0.921	0.903	0.942	0.926	0.954	0.935
A2A (Affine)	30.42	29.14	32.50	30.67	33.42	31.20	0.922	0.900	0.950	0.932	0.959	0.940
A2A (SyN)	32.70	30.31	32.71	30.35	32.85	30.39	0.952	0.929	0.957	0.932	0.956	0.933
A2A (VoxelMorph)	32.44	30.26	33.06	30.67	33.16	31.03	0.950	0.928	0.958	0.936	0.957	0.938
MoDIR	33.71	31.60	33.85	31.67	34.04	31.72	0.962	0.945	0.965	0.947	0.964	0.949
A2A(Oracle)*	34.17	31.89	34.20	31.91	34.29	31.93	0.965	0.948	0.965	0.948	0.966	0.949

*: idealized algorithm, not available in practice.

Table 2: Average PSNR and SSIM values obtained over the testing set. This table demonstrated that MoDIR can achieve comparable performance with respect to A2A(*Oracle*), which, unlike MoRIR, strictly relies on registered data for training. Note that the deformations considered in this table are *in vivo* due to normal aging and disease.

Experiment of Simulated Measurement and Real Deformation				
Schemes	PSNR		SSIM	
	x3	x4	x3	x4
Acceleration rate				
Zero-Filled (ZF)	27.85	25.70	0.757	0.702
Total Variation	32.72	29.49	0.943	0.892
A2A(Unregistered)	31.94	30.05	0.953	0.932
A2A(Affine)	29.97	28.87	0.944	0.925
A2A(SyN)	30.66	28.88	0.947	0.921
A2A(VoxelMorph)	30.36	28.97	0.943	0.927
MoDIR	33.23	31.19	0.966	0.949
A2A(Oracle)*	33.85	31.52	0.966	0.949

*: unreachable without registered measurements.

4.1 Setup

4.1.1 Baseline Methods

We use several image reconstruction methods as references. They can be divided into three categories.

- **Registration-free methods:**

1. *TV*: The traditional total variation regularization method summarized in (4). The classical TV is a learning-free method that requires no registration.
2. *A2A (Unregistered)*: The most basic variant of A2A, trained directly on unregistered measurements. It can be interpreted as the worst-case scenario for MoDIR when no motion-compensation is performed during training.

- **Pre-registration methods:** In this category, we explore the potential of first pre-registering corrupted images and using them for A2A training.

3. *A2A (Affine)*: Uses Affine algorithms implemented in *advanced normalization tools (ANTS)* [59].
4. *A2A (SyN)*: Is similar to *A2A (Affine)*, but uses *Symmetric Normalization (SyN)* [57] algorithm instead.
5. *A2A (VoxelMorph)*: Uses a deep registration method, *VoxelMorph* [29], pre-trained on artifact-corrupted images.

- **Oracle-registration method:**

6. *A2A (Oracle)*: A2A (Oracle) is the idealized variant of MoDIR using the registration model that provides perfect results. In our implementation, we synthesized the *registered* data by applying different deformations and measurement operators on the same ground-truth image. Note that this method is inapplicable to the experimental data as the fully sampled data is unavailable.

4.1.2 Evaluation Metrics

In simulations, we implemented two widely used quantitative metrics, *peak signal-to-noise ratio (PSNR)*, measured in decibels (dB) and *structural similarity index (SSIM)*, relative to the ground-truth images used to synthesize the measurements. On the experimental data, however, our evaluations are qualitative due to the ground truth being unavailable.

4.1.3 Implementation

We have experimented with several choices of \mathcal{L} in (10). The best empirical results were obtained when using the ℓ_1 loss for the experimentally collected measurements, and the Huber function (or smooth- ℓ_1 loss [60]) for the simulated measurements. We performed all our experiments on a machine equipped with an Intel Xeon Gold 6130 Processor and an NVIDIA GeForce RTX 2080 Ti GPU.

4.2 Simulated Measurements and Deformations

4.2.1 Dataset

We used the T1-weighted MR brain acquisitions of 60 subjects obtained from the open dataset OASIS-3 [61] as the raw ground truth for simulating measurements. These 60 subjects were split into 48, 6, and 6 for training, validation, and testing, respectively. For each subject, we extracted the middle 50 to 70 (depending on the shape of the brain) out of the 256 slices on the transverse plane, containing the most relevant regions of the brain. Each slice corresponds to x^r in (8a). We synthesized motion fields ($\phi^{r \rightarrow m}$ in (8b)) based on the method in [58] and used them to deform the ground-truth images, where the resulting images correspond

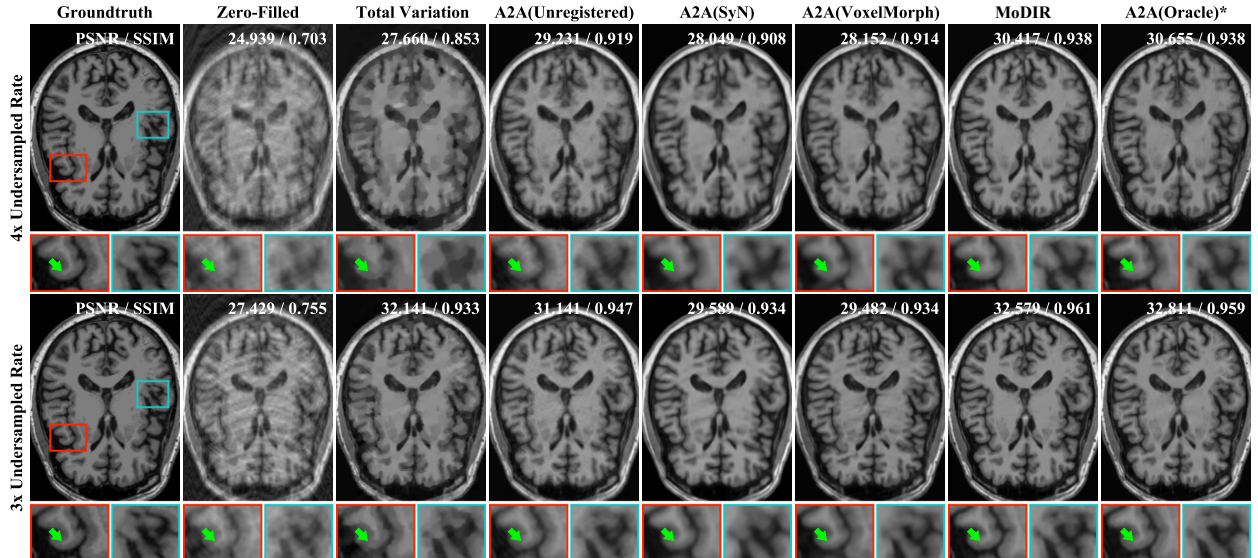


Figure 4: Illustration of several reconstruction methods on simulated MRI measurements under *in vivo* longitudinal deformations and two undersampling rates as 25% (top) and 33% (bottom). The top-right corner of each image provides the PSNR and SSIM values with respect to corresponding ground-truth image. The visual differences are highlighted in the bounding boxes using green arrows. *A2A (Unregistered)* is directly trained on unregistered measurements, while *A2A (SyN)* and *A2A (VoxelMorph)* perform pre-registration on artifact-corrupted images. This figure highlights that MoDIR can achieve competitive performance relative to other baselines, especially to *A2A (Oracle)* that requires registered measurements.

to x^m in (8b). Three pre-defined parameters of the generation were the number of points randomly selected in the zero vector field $p = 2000$, the range of random values assigned to those points $\delta = [-10, 10]$, and the standard deviations of the smoothing Gaussian kernel for the vector field $\sigma \in \{10, 18, 24\}$. Thus, σ is inversely related to the strength of deformation in the image. Fig. 3 shows visual examples of the deformed images generated by synthetic registration fields with different values of σ . In order to obtain corrupted measurement pairs, we simulated a single-coil MRI setting with a Cartesian under-sampling pattern. We set the sampling rate to 25% and 33% (corresponding to $4\times$ and $3\times$ acceleration) of the full sampling rate for the complete k-space data and added measurement noise corresponding to an input SNR of 40dB.

4.2.2 Results

We summarized the quantitative results on the testing set in Table 1. Notably, MoDIR achieved the highest PSNR and SSIM values compared to several reference methods in all setups of deformation strengths and undersampling ratios. Additionally, pre-registering the data before training leads to sub-optimal reconstruction performance. Table 1 also demonstrates that MoDIR can achieve comparable performances with respect to *A2A (Oracle)*, which, unlike MoRID, uses the true deformation.

4.3 Simulated Measurements and Real Deformations

4.3.1 Dataset

We consider a data acquisition scheme that is similar to that described in Sec. 4.2, but differs in the approach to deform the ground truth. Specifically, we used the second MR acquisitions of the 60 subjects from the OASIS-3 [61] dataset as the deformed images. The intervals between the two MR sessions of each subject range from one to ten years. Note that the deformations occurring in two different *in vivo* MR images of

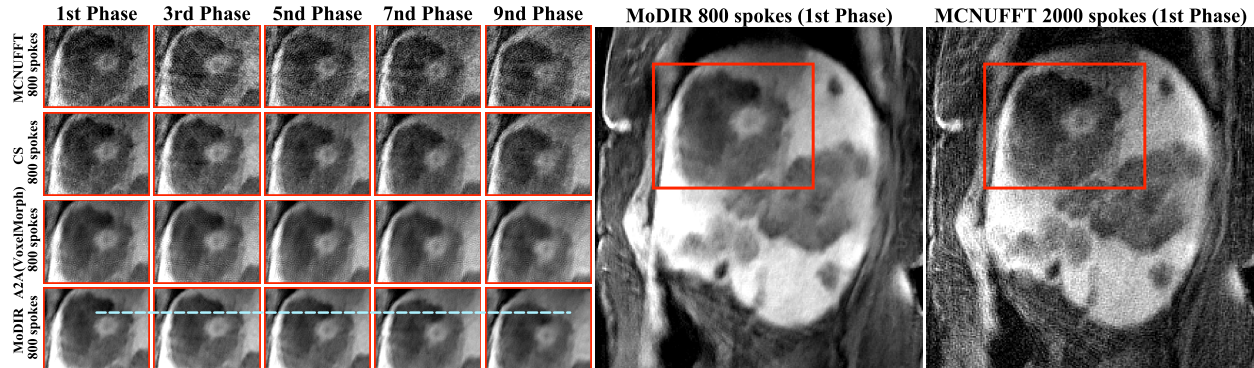


Figure 5: Illustration of *in vivo* respiratory deformation and several 3D reconstruction results from experimentally collected measurements corresponding to 800 spokes (about 2 minutes scan). The blue line provides a horizontal position reference of the tumor in the reconstruction result of MoDIR, demonstrating nonrigid deformations between images across different respiratory phases. While *A2A(VoxelMorph)* trains two networks for image reconstruction and registration separately, this figure shows that MoDIR can universally achieve high-quality results over different respiratory phases by jointly addressing the problem of image reconstruction and registration.

the same subject are due to normal aging and the potential effects of the Alzheimer disease. Fig. 3 visually illustrates the corresponding deformation.

4.3.2 Results

Fig. 4 shows some results over two undersampling rates: 25% (top) and 33% (bottom). One can observe a significant reduction in the amount of imaging artifacts due to *TV* compared to the Zero-Filled reconstruction. However, *TV* also leads to a loss of detail due to the well-known “staircase effect”. While *A2A(Unregistered)* leads to reasonable results even without any registration during training, it also contains a noticeable amount of blur, especially along the edges. Pre-registration methods, such as *A2A(VoxelMorph)*, lead to a significant improvements over the registration-free methods by using pre-registered artifact-contaminated images, but they still suffer from smoothing in the region indicated by the green arrows. Furthermore, MoDIR achieved better performance compared to all of these baseline methods in terms of sharpness, contrast, and artifact removal, due to its ability to simultaneously address problems of image registration and reconstruction during network training. Note that although the measurements were simulated in this experiment for quantitative evaluation, the deformations employed are *in vivo*.

4.4 Real Measurements and Real Deformations

4.4.1 Dataset

All acquisition processes were performed on a 3T PET/MRI scanner (Biograph mMR; Siemens Healthcare, Erlangen, Germany). We collected the data by using the CAPTURE method, a T1-weighted stack-of-stars 3D spoiled gradient-echo sequence with fat suppression that has consistently acquired projections for respiratory motion detection [62]. The acquisition parameters were as follows: TE/TR = 1.69ms/3.54ms, FOV = 360mm × 360mm, in-plane resolution = 1.125 × 1.125mm, partial Fourier factor = 6/8, number of radial spokes = 2000, slice resolution = 50%, slice per slab $N_z = \{96, 112, 120\}$ so as to cover the torso with a slice thickness of 3mm, total acquisition time was about 5 minutes (slightly longer for larger subjects). We discarded the first ten spokes during reconstruction to ensure the acquired signal reached a steady state. Our free-breathing MRI data were subsequently binned into $N_p = 10$ respiratory phases, and thus each phase was reconstructed with $N_s = 199$ spokes. The dimension of raw measurement for each subject was $N_z \times N_c \times N_p \times N_s \times N_l$ with $N_c = \{5, 6\}$ being the number of coils and N_l being the length of radial spokes. The coil sensitivity maps were estimated from the central radial k-space spokes of each slice and

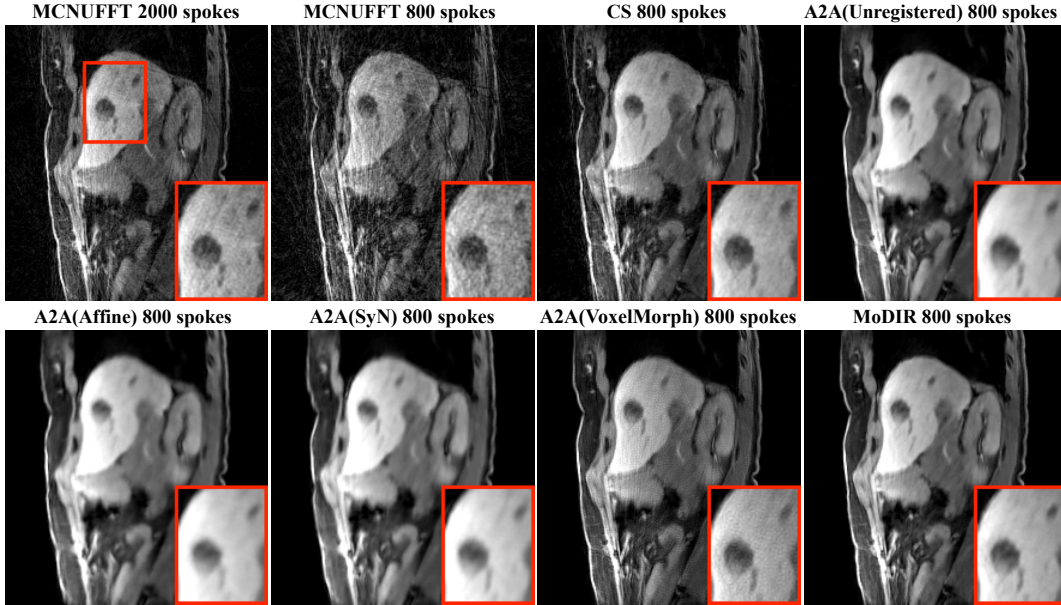


Figure 6: Illustration of several reconstruction results from experimentally collected data corresponding to 800 radial spokes (scans of about 2 minutes). *A2A(Unregistered)* is directly trained on unregistered 3D measurement pairs, while *A2A(SyN)* and *A2A(VoxelMorph)* train CNNs on pre-registered but artifact-corrupted images. *MCNUFFT 2000-spokes* requires data corresponding to 2000 radial spokes (scans of about 5 minutes). This figure highlights that MoDIR can achieve competitive performance relative to other baselines.

were assumed to be known during experiments. Apodization was applied by using a Hamming window that covered the central k-space in order to avoid Gibbs ringing. We used inverse Multi-Coil Non-Uniform Fast Fourier Transform (MCNUFFT) [63] to map those measurements from k-space to the image domain, yielding 4D images $N_x \times N_y \times N_p \times N_z$ for each subject where $N_x \times N_y$ is the image domain matrix size.

Upon the approval of our Institutional Review Board, multichannel liver data from ten healthy volunteers and six cancer patients were used in this paper, where eight healthy subjects were used for training, one healthy subject for validation, and the rest for testing. Raw measurements of each subject were first reformatted into N_z measurements, yielding $8N_z$ samples for training and N_z for validation. We then trained MoDIR on measurement pairs such that each pair contained the five odd phases and the five even phases of the same training sample. Fig. 5 shows examples of MCNUFFT images obtained from a training sample, demonstrating that MoDIR was trained on unregistered measurement pairs corresponding to images with nonrigid respiratory deformations. We used MCNUFFT images from the full acquisition duration (5 minutes) as the reference for qualitative evaluations. We conducted the experiments for various acquisition durations of 1-, 2-, 3-, 4-, and 5-minute, corresponding to 400, 800, 1200, 1600, and 2000 radial spokes in k-space, respectively. Additionally, we replaced the baseline *TV* with the *CS* method from [62].

4.4.2 Results

Fig. 6 illustrates reconstruction results for 800 radial spokes (corresponding to 2 minutes acquisition). Among these results, the MCNUFFT image contains strong streaking artifacts and noise. All other methods yield significant improvements over MCNUFFT. While *CS* shows a considerable reduction in the streaking artifacts, it also contains a noticeable amount of blurring. *A2A(Unregistered)* leads to a reasonable result even without registration in training, but it also contains a noticeable amount of blur, especially along the edges. *A2A(Affine)* and *A2A(SyN)* also suffer from smoothing in the region of interest even with the registration algorithms integrated to pre-align the samples. Note the reduction in blur in *A2A(VoxelMorph)*

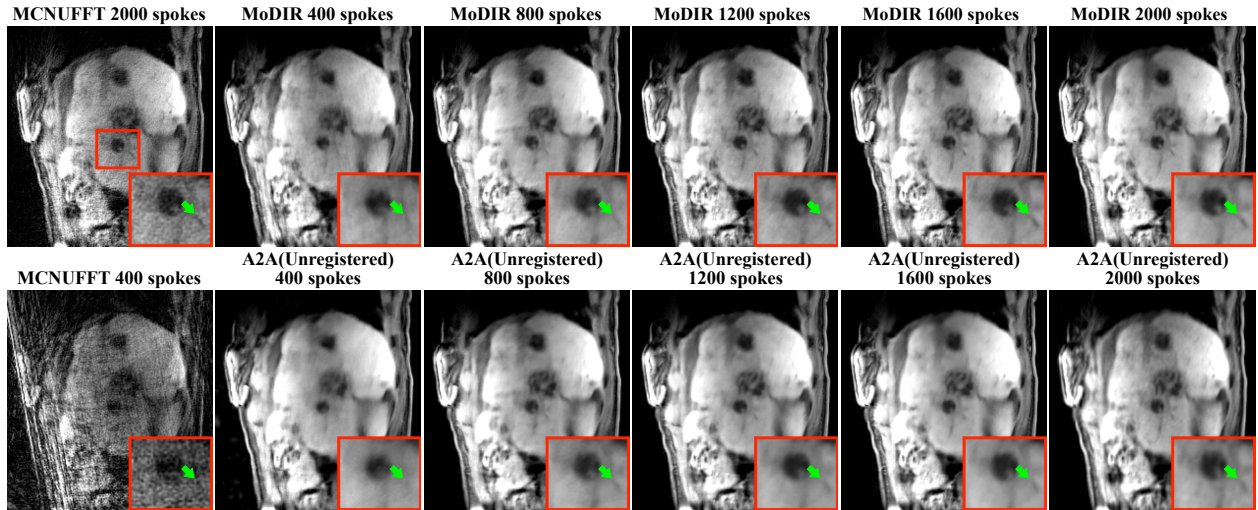


Figure 7: Illustration of reconstruction results of MoDIR and $A2A(Unregistered)$ from experimentally collected measurements using 400, 800, 1200, 1600, and 2000 spokes, which corresponds to 1-, 2-, 3-, 4-, and 5- minute scans, respectively. The visual differences are highlighted in the bounding boxes using green arrows. While $A2A(Unregistered)$ trains CNN directly on unregistered measurements, this figure shows that MoDIR can generally achieve essential improvements over $A2A(Unregistered)$ for different acquisitions durations, by integrating two CNNs for 3D image reconstruction and registration.

relative to the registration-free methods. However, a closer inspection indicates that $A2A(VoxelMorph)$ result still suffers from artifacts. Fig. 6 depicts that MoDIR leads to improvements over several baseline methods, especially compared with $MCNUFFT 2000$ spokes with a longer acquisitions time (5 minutes). Fig. 5 also provides visual comparisons between MoDIR and $A2A(VoxelMorph)$, where MoDIR performs better across different respiratory phases. Note that both the measurements and the deformations in these results are from experimentally collected data, demonstrating the applicability of MoDIR in motion-compensated MRI.

Fig. 7 illustrates comparisons between $A2A(Unregistered)$ and MoDIR for various acquisition durations. We annotated visual differences in the bounding boxes using green arrows. While $A2A(Unregistered)$ trains CNNs directly on unregistered measurement pairs, MoDIR achieves a significant improvement over $A2A(Unregistered)$ by taking into account the motion field during training. Moreover, this figure indicates the benefit of using MoDIR across different acquisition durations.

4.5 Deep Registration Component of MoDIR

In this section, we evaluate the deep registration component of MoDIR, which was trained directly on sub-sampled and noisy data. We consider simulated measurements described in Sec. 4.2 and Sec. 4.3.

4.5.1 Baseline Methods

We used several image registration methods as references that can be divided into three categories.

- **Reconstruction-free methods:** Both methods apply registration algorithms directly on zero-filled (ZF) images.
 1. *Affine (ZF)*: Uses the Affine algorithm implemented in *advanced normalization tools (ANTs)* [59].
 2. *SyN (ZF)*: Similar to *Affine (ZF)*, but uses the *SyN* [57] algorithm instead.
 3. *VoxelMorph (ZF)*: Trains a deep *VoxelMorph* [29] model.

- **Pre-reconstruction methods:**

4. *SyN (TV)*: Uses SyN on images reconstructed using *TV*.

- **Oracle-reconstruction method:**

5. *VoxelMorph (Oracle)*: Similar to *VoxelMorph (ZF)*, but uses clean images for training.

4.5.2 Evaluation Metrics

We implemented Dice Score [64] as the evaluation metric that quantifies the overlap of anatomical segmentation maps generated through Freesurfer [65] between the registered images and their registration targets.

4.5.3 Results

The quantitative results over the test set are summarized in Table 3. This table illustrates that MoDIR can achieve a significant quality improvement when performing deformable corrupted image registration by taking advantage of the concurrent deep image reconstruction.

Table 3: Dice Score obtained over on the testing set. Note that *VoxelMorph(Oracle)* uses ground-truth images as inputs, while the others rely on corrupted counterparts. The highest Dice Scores among methods using corrupted images are in bold. This table illustrates that MoDIR is appropriate to train an end-to-end registration network on corrupted image pairs.

Experiment of Deformable Corrupted Image Registration								
<i>Schemes</i>	Dice Score							
<i>Deformation</i>	Synthetic with $\sigma =$						Longitudinal	
	10		18		24			
<i>Acceleration rate</i>	x3	x4	x3	x4	x3	x4	x3	x4
Unregistered	0.681		0.786		0.837		0.739	
VoxelMorph (ZF)	0.848	0.809	0.903	0.873	0.906	0.891	0.831	0.814
Affine(ZF)	0.684	0.683	0.802	0.799	0.860	0.855	0.811	0.803
SyN (ZF)	0.866	0.815	0.897	0.851	0.850	0.852	0.839	0.801
SyN (TV)	0.899	0.859	0.939	0.898	0.943	0.902	0.860	0.835
MoDIR	0.895	0.863	0.941	0.911	0.945	0.925	0.861	0.844
VoxelMorph (Oracle)*	0.939		0.973		0.983		0.871	

*: unavailable without ground-truth images.

5 Conclusion

We proposed a new method for addressing an important issue in the context of training of deep neural networks for medical image reconstruction. Our proposed MoDIR method extends the influential Noise2Noise approach by working directly in the measurement domain and compensating for object motion in the data. We validated our method using simulated and experimentally collected MRI data. Our results demonstrated that MoDIR significantly improve image quality compared to several baseline methods. While our experiments focused on MRI, the MoDIR method has the potential to be adopted in other imaging modalities as well, such as computerized tomography [27] and optical diffraction tomography [66], where it is often impossible to obtain fully-sampled measurements, but only several distinct views of the object.

6 Acknowledgments

Research reported in this publication was supported by the NSF CAREER award under CCF-2043134 and the Washington University Institute of Clinical and Translational Sciences grant UL1TR002345 from the National Center for Advancing Translational Sciences (NCATS) of the National Institutes of Health (NIH).

References

- [1] M. Lustig, D. Donoho, and J. M. Pauly, “Sparse MRI: The application of compressed sensing for rapid MR imaging,” *Magn. Reson. Med.*, vol. 58, no. 6, pp. 1182–1195, 2007.
- [2] J. Liu, Y. Sun, C. Eldeniz, W. Gan, H. An, and U. S. Kamilov, “RARE: Image Reconstruction using Deep Priors Learned without Ground Truth,” *IEEE J. Sel. Top. Signal Process.*, 2020.
- [3] A. Danielyan, V. Katkovnik, and K. Egiazarian, “BM3D frames and variational image deblurring,” *IEEE Trans. Image Process.*, vol. 21, no. 4, pp. 1715–1728, 2011.
- [4] M. Elad and M. Aharon, “Image denoising via sparse and redundant representations over learned dictionaries,” *IEEE Trans. Image Process.*, vol. 15, no. 12, pp. 3736–3745, 2006.
- [5] Y. Hu, S. G. Lingala, and M. Jacob, “A fast majorize–minimize algorithm for the recovery of sparse and low-rank matrices,” *IEEE Trans. Image Process.*, vol. 21, no. 2, pp. 742–753, 2011.
- [6] L. I. Rudin, S. Osher, and E. Fatemi, “Nonlinear total variation based noise removal algorithms,” *Physica D*, vol. 60, no. 1-4, pp. 259–268, 1992.
- [7] F. Knoll, K. Hammernik, C. Zhang, S. Moeller, T. Pock, D. K. Sodickson, and M. Akcakaya, “Deep-learning methods for parallel magnetic resonance imaging reconstruction: A survey of the current approaches, trends, and issues,” *IEEE Signal Process. Mag.*, vol. 37, no. 1, pp. 128–140, 2020.
- [8] A. Lucas, M. Iliadis, R. Molina, and A. K. Katsaggelos, “Using deep neural networks for inverse problems in imaging: Beyond analytical methods,” *IEEE Signal Process. Mag.*, vol. 35, no. 1, pp. 20–36, 2018.
- [9] M. T. McCann, K. H. Jin, and M. Unser, “Convolutional neural networks for inverse problems in imaging: A review,” *IEEE Signal Process. Mag.*, vol. 34, no. 6, pp. 85–95, 2017.
- [10] G. Ongie, A. Jalal, C. A. Metzler, R. G. Baraniuk, A. G. Dimakis, and R. Willett, “Deep learning techniques for inverse problems in imaging,” *IEEE J. Sel. Areas Inf. Theory*, vol. 1, no. 1, pp. 39–56, 2020.
- [11] G. Wang, J. C. Ye, and B. De Man, “Deep learning for tomographic image reconstruction,” *Nat. Mach. Intell.*, vol. 2, no. 12, pp. 737–748, Dec. 2020.
- [12] M. Akçakaya, B. Yaman, H. Chung, and J. C. Ye, “Unsupervised deep learning methods for biological image reconstruction,” *arXiv:2105.08040*, 2021.
- [13] J. Lehtinen, J. Munkberg, J. Hasselgren, S. Laine, T. Karras, M. Aittala, and T. Aila, “Noise2Noise: Learning image restoration without clean data,” in *Proc. Int. Conf. Machine Learning*, 2018.
- [14] A. Krull, T.-O. Buchholz, and F. Jug, “Noise2void-learning denoising from single noisy images,” in *Proc. IEEE Conf. Computer Vision and Pattern Recognition*, 2019, pp. 2129–2137.
- [15] B. Yaman, S. A. H. Hosseini, S. Moeller, J. Ellermann, K. Uğurbil, and M. Akçakaya, “Self-supervised physics-based deep learning MRI reconstruction without fully-sampled data,” in *Proc. Int. Symp. Biomedical Imaging*, 2020, pp. 921–925.

- [16] S. Laine, T. Karras, J. Lehtinen, and T. Aila, “High-quality self-supervised deep image denoising,” *Advances in Neural Information Processing Systems*, vol. 32, pp. 6970–6980, 2019.
- [17] C. Eldeniz, W. Gan, S. Chen, T. J. Fraum, D. R. Ludwig, Y. Yan, J. Liu, T. Vahle, U. B. Krishnamurthy, U. S. Kamilov, and H. An, “Phase2Phase: Respiratory Motion-Resolved Reconstruction of Free-Breathing MRI Using Deep Learning Without a Ground Truth for Improved Liver Imaging,” *Invest. Radiol.*, 2021.
- [18] M. Torop, S. V. Kothapalli, Y. Sun, J. Liu, S. Kahali, D. A. Yablonskiy, and U. S. Kamilov, “Deep learning using a biophysical model for robust and accelerated reconstruction of quantitative, artifact-free and denoised images,” *Magn. Reson. Med.*, vol. 84, no. 6, pp. 2932–2942, 2020.
- [19] T. Ehret, A. Davy, J. Morel, G. Facciolo, and P. Arias, “Model-blind video denoising via frame-to-frame training,” in *Proc. IEEE Conf. Computer Vision and Pattern Recognition*, 2019, pp. 11 369–11 378.
- [20] S. Yu, B. Park, J. Park, and J. Jeong, “Joint learning of blind video denoising and optical flow estimation,” in *Proc. IEEE Conf. Computer Vision and Pattern Recognition Workshops*, 2020, pp. 500–501.
- [21] Z. Jiang, Z. Huang, B. Qiu, X. Meng, Y. You, X. Liu, M. Geng, G. Liu, C. Zhou, K. Yang *et al.*, “Weakly supervised deep learning-based optical coherence tomography angiography,” *IEEE Trans. Med. Imaging*, vol. 40, no. 2, pp. 688–698, 2020.
- [22] T.-O. Buchholz, M. Jordan, G. Pignino, and F. Jug, “Cryo-CARE: Content-Aware Image Restoration for Cryo-Transmission Electron Microscopy Data,” in *Proc. Int. Symp. Biomedical Imaging*, Apr. 2019, pp. 502–506.
- [23] A. A. Hendriksen, D. M. Pelt, and K. J. Batenburg, “Noise2Inverse: Self-Supervised Deep Convolutional Denoising for Tomography,” *IEEE Trans. Comput. Imaging*, vol. 6, pp. 1320–1335, 2020.
- [24] J. Xu and E. Adalsteinsson, “Deformed2self: Self-supervised denoising for dynamic medical imaging,” *arXiv:2106.12175*, 2021.
- [25] Y. Fu, Y. Lei, T. Wang, W. J. Curran, T. Liu, and X. Yang, “Deep learning in medical image registration: A review,” *Phys. Med. Biol.*, vol. 65, no. 20, p. 20TR01, 2020.
- [26] B. D. de Vos, F. F. Berendsen, M. A. Viergever, H. Sokooti, M. Staring, and I. Išgum, “A deep learning framework for unsupervised affine and deformable image registration,” *Med. Image Anal.*, vol. 52, pp. 128–143, 2019.
- [27] Y. Lei, Y. Fu, J. Harms, T. Wang, W. J. Curran, T. Liu, K. Higgins, and X. Yang, “4d-ct deformable image registration using an unsupervised deep convolutional neural network,” in *Artificial Intelligence in Radiation Therapy*, 2019, pp. 26–33.
- [28] I. Yoo, D. G. Hildebrand, W. F. Tobin, W.-C. A. Lee, and W.-K. Jeong, “ssEMnet: Serial-section electron microscopy image registration using a spatial transformer network with learned features,” in *Deep Learning in Medical Image Analysis and Multimodal Learning for Clinical Decision Support*, 2017, pp. 249–257.
- [29] G. Balakrishnan, A. Zhao, M. R. Sabuncu, J. Guttag, and A. V. Dalca, “Voxelmorph: A learning framework for deformable medical image registration,” *IEEE Trans. Med. Imaging*, vol. 38, no. 8, pp. 1788–1800, 2019.
- [30] W. Gan, Y. Sun, C. Eldeniz, J. Liu, H. An, and U. S. Kamilov, “Deep Image Reconstruction using Unregistered Measurements without Groundtruth,” *arXiv:2009.13986*, Sep. 2020.
- [31] H. K. Aggarwal, M. P. Mani, and M. Jacob, “MoDL: Model-Based Deep Learning Architecture for Inverse Problems,” *IEEE Trans. Med. Imaging*, vol. 38, no. 2, pp. 394–405, Feb. 2019.

- [32] J. Schlemper, J. Caballero, J. V. Hajnal, A. N. Price, and D. Rueckert, “A Deep Cascade of Convolutional Neural Networks for Dynamic MR Image Reconstruction,” *IEEE Trans. Med. Imaging*, vol. 37, no. 2, pp. 491–503, Feb. 2018.
- [33] Y. Yang, H. Li, J. Sun, and Z. Xu, “Deep ADMM-Net for Compressive Sensing MRI,” in *Advances in Neural Information Processing Systems*, 2016, p. 9.
- [34] O. Ronneberger, P. Fischer, and T. Brox, “U-net: Convolutional networks for biomedical image segmentation,” in *Proc. Medical Image Computing and Computer-Assisted Intervention*, 2015, pp. 234–241.
- [35] S. V. Venkatakrisnan, C. A. Bouman, and B. Wohlberg, “Plug-and-play priors for model based reconstruction,” in *Proc. IEEE Global Conf. Signal Process. and Inf. Process. (GlobalSIP)*, 2013, pp. 945–948.
- [36] Y. Romano, M. Elad, and P. Milanfar, “The little engine that could: Regularization by denoising (red),” *SIAM J. Imaging Sci.*, vol. 10, no. 4, pp. 1804–1844, 2017.
- [37] S. Sreehari, S. V. Venkatakrisnan, B. Wohlberg, G. T. Buzzard, L. F. Drummy, J. P. Simmons, and C. A. Bouman, “Plug-and-play priors for bright field electron tomography and sparse interpolation,” *IEEE Trans. Comp. Imag.*, vol. 2, no. LA-UR-15-28750, 2016.
- [38] K. Zhang, W. Zuo, S. Gu, and L. Zhang, “Learning deep cnn denoiser prior for image restoration,” in *Proc. IEEE Conf. Computer Vision and Pattern Recognition*, 2017, pp. 3929–3938.
- [39] Y. Sun, S. Xu, Y. Li, L. Tian, B. Wohlberg, and U. S. Kamilov, “Regularized fourier ptychography using an online plug-and-play algorithm,” in *Proc. IEEE Int. Conf. Acoustics, Speech and Signal Process. (ICASSP)*. IEEE, 2019, pp. 7665–7669.
- [40] K. Zhang, W. Zuo, and L. Zhang, “Deep plug-and-play super-resolution for arbitrary blur kernels,” in *Proc. IEEE Conf. Computer Vision and Pattern Recognition*, 2019, pp. 1671–1681.
- [41] R. Ahmad, C. A. Bouman, G. T. Buzzard, S. Chan, S. Liu, E. T. Reehorst, and P. Schniter, “Plug-and-play methods for magnetic resonance imaging: Using denoisers for image recovery,” *IEEE Signal Process. Mag.*, vol. 37, no. 1, pp. 105–116, 2020.
- [42] K. Gregor and Y. LeCun, “Learning fast approximations of sparse coding,” in *Proc. Int. Conf. Machine Learning*, 2010, pp. 399–406.
- [43] J. Zhang and B. Ghanem, “Ista-net: Interpretable optimization-inspired deep network for image compressive sensing,” in *Proc. IEEE Conf. Computer Vision and Pattern Recognition*, 2018, pp. 1828–1837.
- [44] Y. Chen, W. Yu, and T. Pock, “On learning optimized reaction diffusion processes for effective image restoration,” in *Proc. IEEE Conf. Computer Vision and Pattern Recognition*, 2015, pp. 5261–5269.
- [45] J. Liu, Y. Sun, W. Gan, X. Xu, B. Wohlberg, and U. S. Kamilov, “Sgd-net: Efficient model-based deep learning with theoretical guarantees,” *IEEE Trans. Comput. Imag.*, 2021.
- [46] A. Krull, T. Vičar, M. Prakash, M. Lalit, and F. Jug, “Probabilistic Noise2Void: Unsupervised content-aware denoising,” *Frontiers in Computer Science*, vol. 2, Feb. 2020.
- [47] J. Batson and L. Royer, “Noise2self: Blind denoising by self-supervision,” in *Proc. Int. Conf. Machine Learning*, 2019, pp. 524–533.
- [48] S. Soltanayev and S. Y. Chun, “Training deep learning based denoisers without ground truth data,” in *Advances in Neural Information Processing Systems*, 2018, p. 11.
- [49] Y. Quan, M. Chen, T. Pang, and H. Ji, “Self2Self With Dropout: Learning Self-Supervised Denoising From Single Image,” in *Proc. IEEE Conf. Computer Vision and Pattern Recognition*, Jun. 2020, pp. 1887–1895.

- [50] X. Yang, P. Ghafourian, P. Sharma, K. Salman, D. Martin, and B. Fei, “Nonrigid registration and classification of the kidneys in 3d dynamic contrast enhanced (dce) mr images,” in *Proc. SPIE Int. Soc. Opt. Eng.*, vol. 8314, 2012, p. 83140B.
- [51] X. Han, M. S. Hoogeman, P. C. Levendag, L. S. Hibbard, D. N. Teguh, P. Voet, A. C. Cowen, and T. K. Wolf, “Atlas-based auto-segmentation of head and neck ct images,” in *Proc. Medical Image Computing and Computer-Assisted Intervention*, 2008, pp. 434–441.
- [52] Y. Fu, S. Liu, H. H. Li, and D. Yang, “Automatic and hierarchical segmentation of the human skeleton in ct images,” *Phys. Med. Biol.*, vol. 62, no. 7, p. 2812, 2017.
- [53] R. Bajcsy and S. Kovačič, “Multiresolution elastic matching,” *Comput. Vis., Graph., and Image Process.*, vol. 46, no. 1, pp. 1–21, 1989.
- [54] M. Jaderberg, K. Simonyan, and A. Zisserman, “Spatial transformer networks,” in *Advances in Neural Information Processing Systems*, vol. 2, 2015, pp. 2017–2025.
- [55] D. P. Kingma and J. Ba, “Adam: A method for stochastic optimization,” *arXiv:1412.6980*, 2014.
- [56] B. Lim, S. Son, H. Kim, S. Nah, and K. Mu Lee, “Enhanced deep residual networks for single image super-resolution,” in *Proc. IEEE Conf. Computer Vision and Pattern Recognition Workshops*, 2017.
- [57] B. B. Avants, C. L. Epstein, M. Grossman, and J. C. Gee, “Symmetric diffeomorphic image registration with cross-correlation: Evaluating automated labeling of elderly and neurodegenerative brain,” *Med. Image Anal.*, vol. 12, no. 1, pp. 26–41, 2008.
- [58] H. Sokooti, B. De Vos, F. Berendsen, B. P. Lelieveldt, I. Išgum, and M. Staring, “Nonrigid image registration using multi-scale 3D convolutional neural networks,” in *Proc. Medical Image Computing and Computer-Assisted Intervention*, 2017, pp. 232–239.
- [59] B. B. Avants, N. Tustison, and G. Song, “Advanced normalization tools (ants),” *Insight j*, vol. 2, no. 365, pp. 1–35, 2009.
- [60] S. Ren, K. He, R. Girshick, and J. Sun, “Faster r-cnn: Towards real-time object detection with region proposal networks,” *IEEE Trans. Pattern Anal. Mach. Intell.*, vol. 39, no. 6, pp. 1137–1149, 2017.
- [61] P. J. LaMontagne, T. L. Benzinger, J. C. Morris, S. Keefe, R. Hornbeck, C. Xiong, E. Grant, J. Hassenstab, K. Moulder, A. Vlassenko *et al.*, “OASIS-3: Longitudinal neuroimaging, clinical, and cognitive dataset for normal aging and Alzheimer disease,” *MedRxiv 2019.12.13.19014902*, 2019.
- [62] C. Eldeniz, T. Fraum, A. Salter, Y. Chen, H. . Gach, P. Parikh, K. Fowler, and H. An, “Consistently-Acquired Projections for Tuned and Robust Estimation—A self-navigated respiratory motion correction approach,” *Invest. Radiol.*, vol. 53, no. 5, p. 293, 2018.
- [63] M. J. Muckley, R. Stern, T. Murrell, and F. Knoll, “TorchKbNufft: A high-level, hardware-agnostic non-uniform fast Fourier transform,” in *ISMRM Workshop on Data Sampling & Image Reconstruction*, 2020.
- [64] L. R. Dice, “Measures of the amount of ecologic association between species,” *Ecology*, vol. 26, no. 3, pp. 297–302, 1945.
- [65] B. Fischl, “FreeSurfer,” *NeuroImage*, vol. 62, no. 2, pp. 774–781, 2012.
- [66] U. S. Kamilov, I. N. Papadopoulos, M. H. Shoreh, A. Goy, C. Vonesch, M. Unser, and D. Psaltis, “Optical tomographic image reconstruction based on beam propagation and sparse regularization,” *IEEE Trans. Comput. Imag.*, vol. 2, no. 1, pp. 59–70, 2016.